MODELING OF NANOSECOND LASER VAPORIZATION AND EXPLOSIVE BOILING OF METALS.

VLADIMIR I. MAZHUKIN[1], ALEXANDER A. SAMOKHIN, MIKHAIL M. DEMIN[1], ALEXANDER V. SHAPRANOV[1]

[1]Keldysh Institute of Applied Mathematics, RAS, Moscow, Russia
e-mail: vim@modhef.ru

[2]A.M. Prokhorov General Physics Institute, RAS, Moscow, Russia

Abstract Nanosecond laser heating of liquid metal film (Al, thickness 430 nm, initial number of particles $5 \cdot 10^5$) from subcritical to supercritical state is investigated in the framework of molecular dynamic simulation combined with a continuum description of conduction band electron system. Calculation results presented for different absorbed laser intensities (38.5, 44, 88 and 154 MW/cm^2) and various heating time durations in the form of sample snapshots as well as temperature, density, pressure and particle velocity distributions. As in the case of dielectric film considered before, it is possible to discriminate four different regimes of film behavior depending on the laser intensity: quasi-stationary regime with surface evaporation, explosive (volume) boiling, spinodal decomposition and supercritical fluid expansion. Appearance of explosive boiling in metals is not evident beforehand because high values of absorption and heat diffusion coefficients strongly impede manifestations of this process. The recoil pressure pulsation due to explosive boiling can be used as a marker of approaching the critical values of parameters in the irradiated sample.

1 INTRODUCTION

In papers [1-3] we considered behavior of a thin (48 nm) dielectric liquid film heated with spatially homogeneous effective energy deposition rates of $2 \div 100$ K/ps. At low heating rates, inertial confinement plays no significant role as compared to surface evaporation which enhances also the explosive boiling process because the temperature maximum T_m in the film exceeds its surface temperature T_s. The maximum value in the temperature distribution diminishes in metals because of the high thermal conductivity value. It was shown [4 cola], however, that explosive boiling in the thin metal film (48 nm) can also develop giving rise to two approximately equal fragments near the process threshold. In more thick samples, explosive boiling can repeat itself as it was predicted forty years ago [5] and recently was confirmed numerically [6]

The laser ablation process is investigated experimentally and theoretically for many decades (see, e.g., [7-20] and references therein). However, investigation of nanosecond laser ablation of metals in the near critical region remains incomplete in many aspects. In this paper, which continues our previous works [1-4, 6] new results describing nonequilibrium phase transition properties are presented.

2 STATEMENT OF THE PROBLEM

We consider a free metal film irradiated by the laser radiation. The problem is reduced to an effectively one-dimensional approximation along the x axis (for the processes of transfer of the laser radiation, energy, momentum and mass) using periodic boundary conditions in the y and z directions. The metal film is considered as two subsystems: electron and ion one with energy exchange between them. The right free surface of the film is irradiated by the laser radiation, which is then absorbed by the electron component and is transferred to the ion subsystem via inelastic collisions.

Combined TTM-MD model is used to describe the processes in the metal film [13,20]. The behavior of the electron subsystem is described using the continuum equation of energy:

$$\frac{\partial \varepsilon_e}{\partial t} = -\left(\frac{\partial W_e}{\partial x} + g(T_e)(T_e - T_{ph}) + \frac{\partial G}{\partial x} \right), \tag{1}$$

$$\frac{\partial G}{\partial x} + \alpha(T_e)G = 0. \tag{2}$$

Here $\varepsilon_e = \varepsilon_e(N_e, T_e) = \int_0^{T_e} C_e(N_e, T_e)dT_e$ is the volumetric density of electron energy, T_e, T_i are the electron and ion temperatures, $g(T_e)$ is the electron-ion coupling coefficient, G_x is the laser radiation flux, $W_e = -\lambda_e(T_e, T_{ph})\frac{\partial T_e}{\partial x}$ is the thermal flux, $\lambda_e(T_e, T_{ph})$ is the coefficient of electron heat conductivity, $\alpha(T_e)$ is the coefficient of volumetric absorption of laser radiation.

Thermophysical and thermodynamic characteristics of the electron Fermi gas for arbitrary temperature are given in Ref. [21], where specific heat C_e, thermal conductivity λ_e and energy coupling coefficient λ_e are written in terms of fundamental physical quantities – electron mean free path l_e and characteristic time (frequency) of interaction τ_e for two scattering mechanisms: electron-electron and electron-phonon.

Specific heat of electron gas $C_e(N_e, T_e)$ can be approximated using Fermi integrals with relative error less than 5% as the following relation:

$$C_e(N_e, T_e) \cong \frac{3}{2} \frac{N_e k_B^2 T_e [K]}{\left[(k_B T_e)^2 + \left(\frac{3\varepsilon_F}{\pi^2} \right)^2 \right]^{\frac{1}{2}}},$$

where $N_e = zN_a$ and z is the number of valence electrons, N_a is the concentration of the lattice atoms (ions).

The obtained expression gives the classical linear temperature dependence of the specific heat of degenerate electron gas in the low temperature region $k_B T_e << \varepsilon_F$, $C_e(N_e, T_e) = \frac{\pi^2}{2} \frac{k_B^2 T_e N_e}{\varepsilon_F}$, and constant value for $k_B T_e >> \varepsilon_F$ corresponding to the specific heat of a gas with the Maxwell distribution $C_e = 3/2k_B N_e$. The dependence $C_e(N_e, T_e)$ for Aluminum is plotted at Fig. 1.
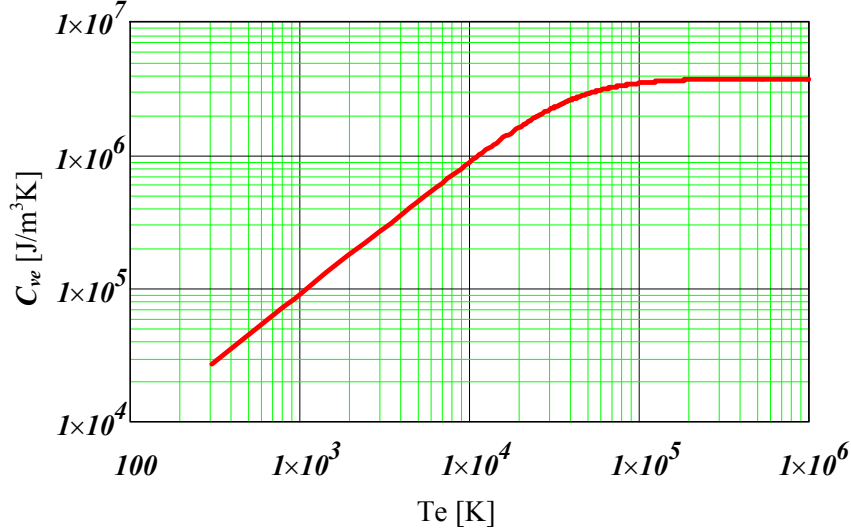
Fig.1. Temperature dependence of electron specific heat $C_e(N_e, T_e)$

Determination of the thermal conductivity of the electron gas is based on a fundamental physical quantity of the mean free path ℓ_e. According to the elementary kinetic theory, thermal conductivity of gas is determined by the expression

$$\left(\lambda_e(T_e, T_{ph})\right)_k = \left(\frac{1}{3} C_e \ell_e(T_e, T_{ph}) <\upsilon_e>\right)_k = \frac{C_e <\upsilon_e>}{3}\left(\frac{\ell_{ee}\,\ell_{eph}}{\left(\ell_{ee}+\ell_{eph}\right)}\right)_{k=s,\ell},$$

where $k = s, l$ is the notation for the solid and liquid phases correspondingly, $<\upsilon_e>$ is the average thermal velocity, $\ell_e(T_e, T_{ph})$ is the averaged electron free path. Electron free path in metals is controlled by the pair electron-electron l_{ee} and electron-phonon collisions ℓ_{eph}.

Electron free path l_{ee} is determined using the gas-dynamic formula

$$l_{ee} = \frac{1}{N_e \sigma_{ee}},$$

where σ_{ee} is the scattering cross-section with transfer of $\Delta\mathcal{E}$ energy value for the electrons with the energies $\mathcal{E}_1, \mathcal{E}_2$.

$$\sigma_{ee} == \frac{2\pi}{9}\left(\frac{4}{9\pi}\right)^{4/3} z^{-4/3}\frac{r^4}{r_B^2}\frac{\xi^2\left[\ln(t+1)-\dfrac{t}{(t+1)}\right]}{\left(\xi^2+\frac{4}{9}\right)\left(\xi^2+0.16\right)},$$

where $\xi = \dfrac{k_B T_e}{\varepsilon_F}$, $t = 4\langle k \rangle^2 d^2 = \left(\dfrac{9\pi}{4}\right)^{4/3} z^{1/3} \dfrac{r_B}{r} \cdot \left[\left(\xi^2 + 0.16\right) \cdot \left(\xi^2 + \dfrac{4}{9}\right)\right]^{1/2}$, $r_B = \dfrac{\hbar^2}{me^2}$ is the

Bohr radius, $r = \left(\dfrac{3}{4\pi N_a}\right)^{1/3}$ is the mean interatomic distance, e, m are the electron change and

mass, $\hbar$ is the Planck constant, d is the radius (Debye) of the field $U = \dfrac{e^2}{r} \exp\left(-\dfrac{r}{d}\right)$.

Electron mean free path l_{ee} is written in terms of σ_{ee} as:

$$l_{ee} = \frac{1}{N_e \sigma_{ee}} = \left[N_e \cdot \frac{2\pi}{9}\left(\frac{4}{9\pi}\right)^{4/3} z^{-4/3} \frac{r^4}{r_B^2} \frac{\xi^2 \left[\ln(t+1) - \dfrac{t}{(t+1)}\right]}{\left(\xi^2 + \frac{4}{9}\right)\left(\xi^2 + 0.16\right)}\right]^{-1} =$$

$$= \frac{2}{\pi^2}\left(\frac{4}{9\pi}\right)^{1/3} \frac{1}{r^2} \frac{1}{z^{1/3} N_a} \cdot \frac{t^2}{\xi^2}\left[\ln(1+t) - \frac{t}{1+t}\right]^{-1}$$

According to calculations, mean free path l_{ee} for Al varies in a wide range of $(\sim 10^{-2} \div 10^{-7})$ cm and has a minimum at $k_B T_e \approx \varepsilon_F$.

Mean free path ℓ_{eph} is determined by the electron-phonon interaction and is described under the assumption of elastic scattering of conduction electrons on the lattice vibrations. It is useful to use the phenomenological approach [22] to determine mean free path ℓ_{eph} in terms of macroscopic values

$$\left[\ell_{eph} = \frac{E \cdot r}{N_e k_B T_{ph}}\right]_{k=s,\ell}$$

where E_k is the Young's modulus of the solid and liquid phases, T_{ph} is the lattice temperature. Melting of the most metals is accompanied by reduction in the elastic modulus by 2-3 times, resulting in an abrupt decrease in the mean free path l_{eph}.

Mean free path l_{eph} calculated for Al decreases by several orders as compared to l_{ee}: by 1.5÷2 orders in the high-temperature region and by 4÷5 orders in the low temperature one.

Mean electron thermal velocity $<\upsilon_e>$ is expressed in terms of its mean energy $<\varepsilon_e>$ as

$$<\upsilon_e> = \left(\frac{2}{m}<\varepsilon_e>\right)^{1/2} = \left(\frac{3\mathcal{E}_F}{m}\left(\xi^2 + 0.16\right)^{1/2}\right)^{1/2} = \left(\frac{3}{2}\right)^{1/2}\left(\frac{9\pi}{4}\right)^{1/3}\frac{z^{1/3}}{r}\frac{\hbar}{m_e}\left(\xi^2 + 0.16\right)^{1/4},$$

The temperature dependence of λ_e for Al is plotted at Fig. 2 for the equilibrium case where $T_e = T_{ph}$. According to the obtained results, electron thermal conductivity $\lambda_e(T_e, T_{ph})$ weakly depends on temperature for the temperature range below the equilibrium boiling temperature and decreases abruptly at the melting point. In the high temperature range, $T_e > 1$eV, thermal conductivity rapidly grows due to domination of the electron-electron scattering. It is quite

natural that in this region, thermal conductivity of electron gas depends on the density of electrons and that λ_e rises with increasing concentration of electrons.
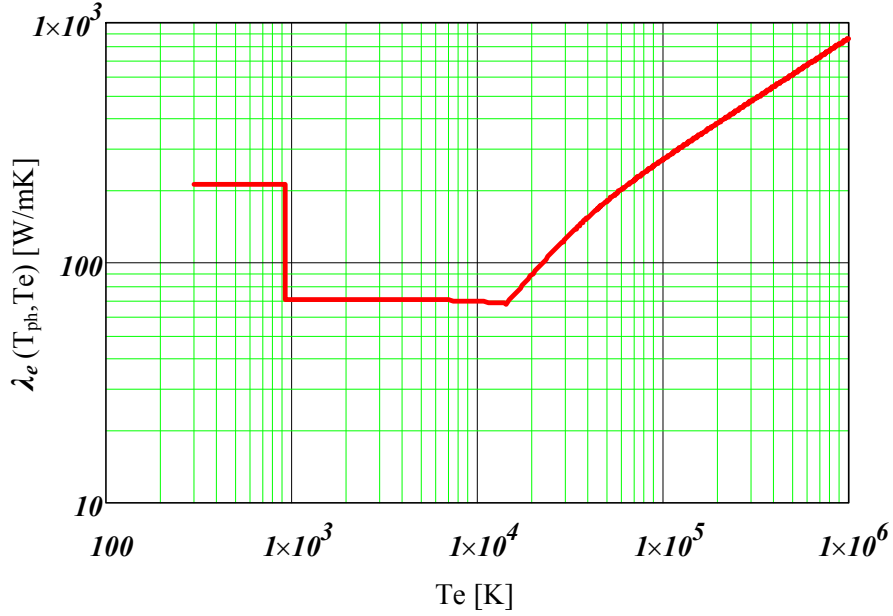

Fig. 2. Temperature dependence of total electron thermal conductivity $\lambda_e(T_e, T_{ph})$

The electron-ion coupling coefficient is written as

$$g(\xi) = \langle \Delta\varepsilon \rangle \frac{k_B N_e}{\varepsilon_F} = \left(\frac{3}{2}\right)^{1/2} \left(\frac{8}{9\pi}\right)^{1/3} \frac{8}{3} \cdot \frac{\hbar k_B}{r_B^2 M_0} \frac{z^2}{A} N_a \left[1 - \left(\frac{1}{2^4 z}\right)\right] \Phi_{eph}(\xi),$$

where

$$\Phi_{eph}(\xi) = \begin{cases} \Phi_{eph}(\xi) = \dfrac{\xi \cdot \left[\ln(t_1+1) - \dfrac{t_1}{(t_1+1)}\right]}{\left(\xi^2 + 0.16\right)^{1/4}\left(\xi^2 + \dfrac{4}{9}\right)^{1/2}} & ,\xi < 1 \\[3em] \Phi_{eph}(\xi) = \dfrac{\xi \cdot \left[\ln(t_1+1) - \dfrac{t_1}{(t_1+1)}\right]}{\left(\xi^2 + 0.16\right)^{3/4}\left(\xi^2 + \dfrac{4}{9}\right)^{1/2}} & ,\xi \geq 1 \end{cases}$$

is a dimensionless function.
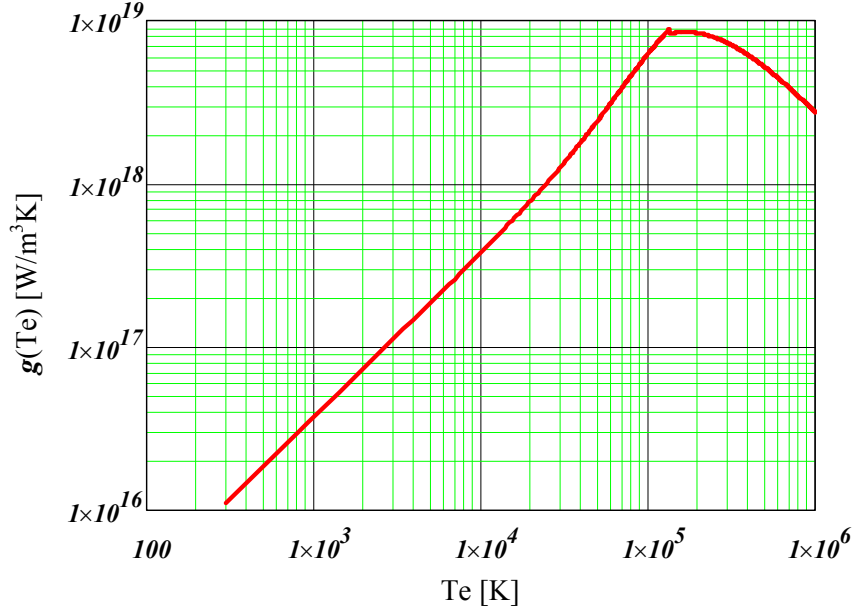
Fig.3. Temperature dependence of electron-ion coupling coefficient $g(T_e)$.

The continuum equations (1), (2) are solved within the condensed matter using an implicit finite-difference scheme. Zero heat flux was used as the boundary conditions on the moving surfaces of the initial film and surfaces of the separated fragments during modeling.

The processes in the ion subsystem were described in the framework of the atomistic model:

$$\begin{cases} \dfrac{d\vec{r}_j}{dt} = \vec{\upsilon}_j \\ m_j \dfrac{d\vec{\upsilon}_j}{dt} = \vec{F}_j^{\,emb} + \vec{G}_j \end{cases} \qquad (3)$$

$$j = 1\ldots N$$

where $m_j, \vec{r}_j, \vec{\upsilon}_j$ are the mass, radius-vector and velocity of the j-th ion correspondingly, $\vec{F}_j^{\,emb} = -\dfrac{\partial U(\vec{r}_1 \ldots \vec{r}_N)}{\partial \vec{r}_j}$ is the force acting on the j-th ion from all other atoms, $U(\vec{r}_1 \ldots \vec{r}_N)$ is the interaction potential, which was used in the form of EAM potential [16]. Electron-ion energy exchange causes addition of an extra force term into the equation of the ion motion:

$$\vec{G}_j = m_j(\vec{\upsilon}_j - \langle \vec{\upsilon} \rangle)\frac{g(T_e)(T_e - T_i)}{3k_B T_i n_i},$$

where k_B is the Boltzmann constant, $\langle \vec{\upsilon} \rangle$ is the mean ion velocity in some neighborhood of j-th atom.

The dimensions of the calculation domain $x \times y \times z$ were set to: $850 \times 6.2 \times 6.2$ nm. The film was located in the center of the domain. Its initial size along the x axis was about 430 nm, which corresponds to the number of particles of 5×10^5.

The initial conditions for the film were chosen at the temperature of $T_e(x,0) = T_{ph}(x,0) = T(x,0) = 6400$K. The boundary conditions for the electron component were set at the moving boundaries of the film: $x_0 = 0$: $\quad W_e(x_0,t) = 0$; $x_L = 430$: $W_e(x_L,t) = 0$, $\quad G(x_L,t) = A(T_e)G_0$, where $A(T_e)$ is the surface absorptance, G_0 is the incident laser intensity. The optical properties $A(T_e)$, $\alpha(T_e)$ were taken from Ref. [23].

Molecular-dynamic equations were solved using Verlet scheme and well-known methods of parallel calculations for the hybrid systems [24] (neighbor-list generation for a short-range potential, domain decomposition and balancing). The calculations were performed using K-100 supercomputer at Keldysh Institute of Applied Mathematics of RAS.

3 RESULTS AND DISCUSSION

First it useful to compare the temperature and density distributions in thin (48 nm) dielectric (Fig. 4) and metal (Fig. 5) films at the beginning of explosive boiling. In the latter case, the distributions have no such pronounced extrema as in the dielectric film but in both cases explosive boiling begins approximately in the middle of the film.
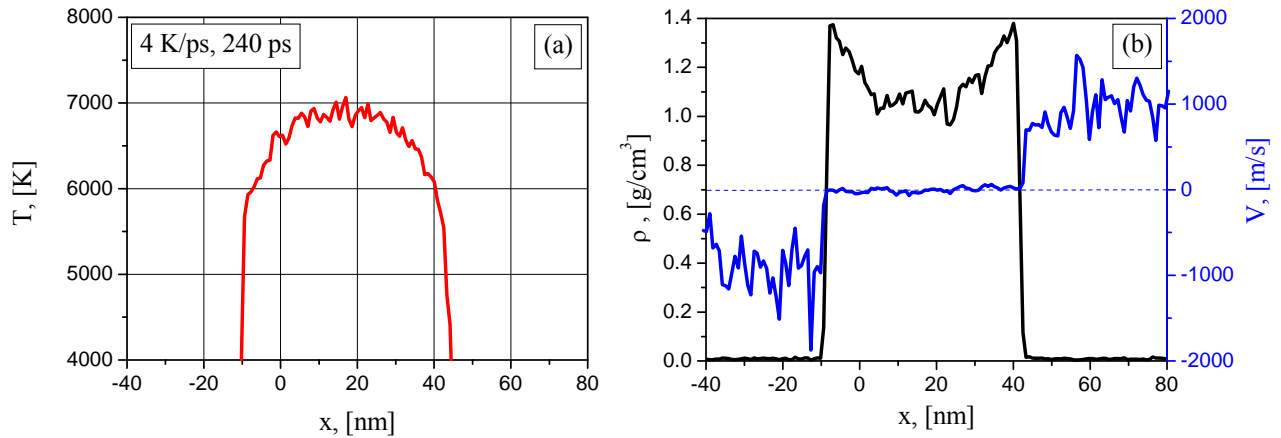
Fig.4. Distributions of dielectric film temperature (a), density (b, black curve) and x-component of particles velocity at 250 ps after the heating beginning with 4 K/ps effective energy deposition rate.

For a thicker film (417 nm) the situation is quite different. All figures below (except for Figs. 12 and 29) show the temperature, density, pressure, velocity and particle distributions in the sample. The distributions are time-averaged over 5 ps interval. Log scales are used in Figs 6-11, 13-18 for the density distributions.

On the right side where laser radiation is absorbed, the film temperature can be considerably higher than on the left side as it is seen from Fig. 6a-11a, Fig.13a-28a. In the limit of very thick evaporating metal films (half space) [8] film temperature maximum T_m location under the irradiated surface approximately coincides with absorption length α^{-1} and the difference

$(T_m - T_s)$ is proportional to the parameter $\delta = v / \alpha\chi$, where v and χ denote the velocity of vaporization front and thermal diffusivity, respectively. For metals, usually δ<<1 even near the critical region if no metal-dielectric transition occurs.
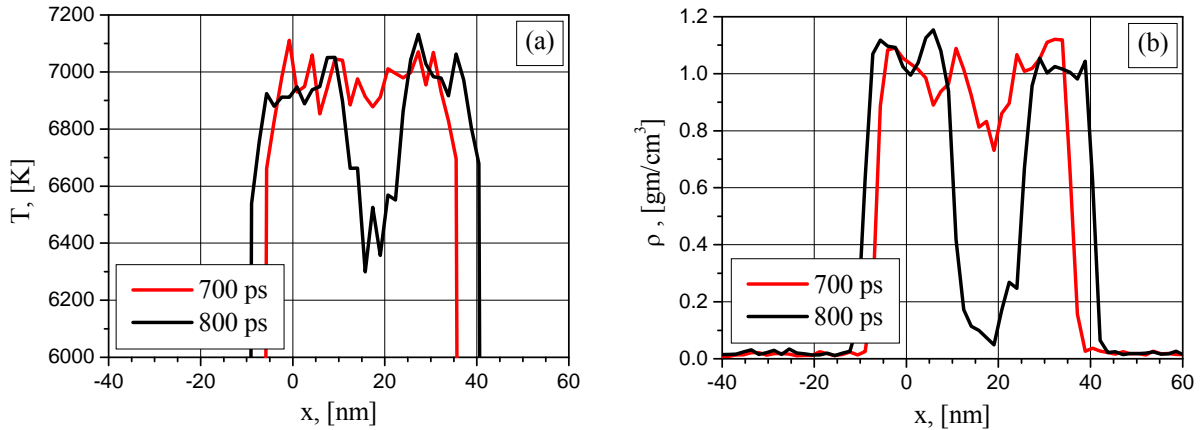

Fig.5. Distributions of metal film temperature (a) and density (b) at 700 ps (red curves) and 800 ps (black curves) after the heating beginning with 5 K/ps effective energy deposition rate.

However, despite above mentioned unfavorable facts, our calculations (Fig. 7-11, 16-18) clearly show the manifestations of repetitive explosive boiling processes, which begin approximately at 1.04 ns, 1.44 ns, 1.64 ns, 2 ns and 2.34 ns for I = 38.5 MW/cm^2 and at 0.71 ns, 1.16 ns, 1.5 ns and 1.79 ns for I = 44 MW/cm^2. Due to this process, thin layers of condensed matter are blown up from the irradiated sample surface. The initial thickness of these thin layers is of the order of α^{-1}, which is approximately as twice as smaller compared to the fragment thickness at Fig.4- Fig.5.

Just before the explosions, one can see the growth of density fluctuations (Fig. 6b) and some "competition" between the growing fluctuations with different localization under the irradiated surface (Fig. 13b – Fig. 16b). From the two prominent density fluctuations (Fig. 13b) only the one nearest to the surface transforms to a growing vapor cavity separating the moving away fragment and the rest part of the film.

At the low laser intensity (38.5 and 44 MW/cm^2), the evolution of fragment density is not monotonous (Figs. 7b, 8b, 11b, 15b, 16b), exceeding at some times the initial density value coinciding with the right side film density. The growing fragment density is more clearly visible in the linear scale with the averaging time interval of 1 ps. (Fig. 12). Such evolution means some stabilization of the fragments providing considerable jumps in the vapor particles density, pressure and velocity distributions (Fig. 8b, 8c,. 8d, 11b, 11c, 11d)

At the higher intensity, no such effect is observed and fragment boundaries become less distinctive as it is seen from Fig. 19b- Fig.24b together with corresponding sample snapshots. This regime can be described as spinodal decomposition which occurs at the subcritical temperature and pressure values with less sharper emerging interphase boundaries than in the explosive boiling case.
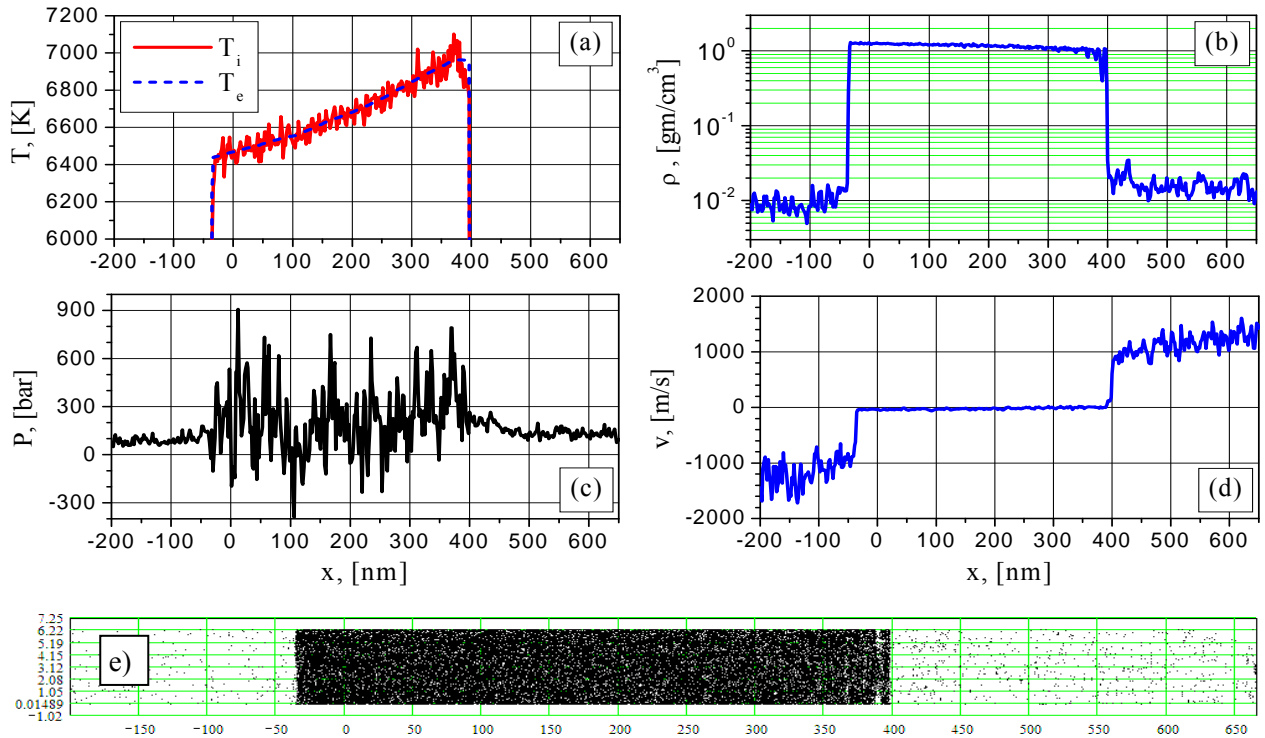
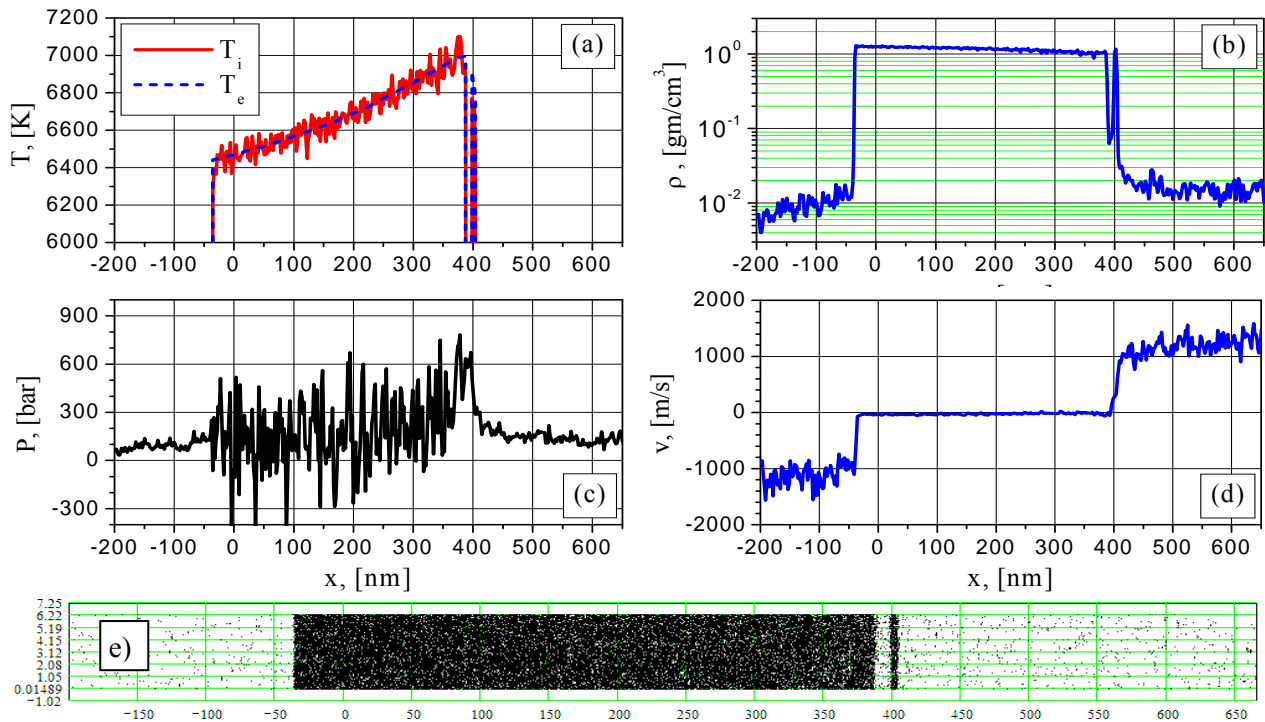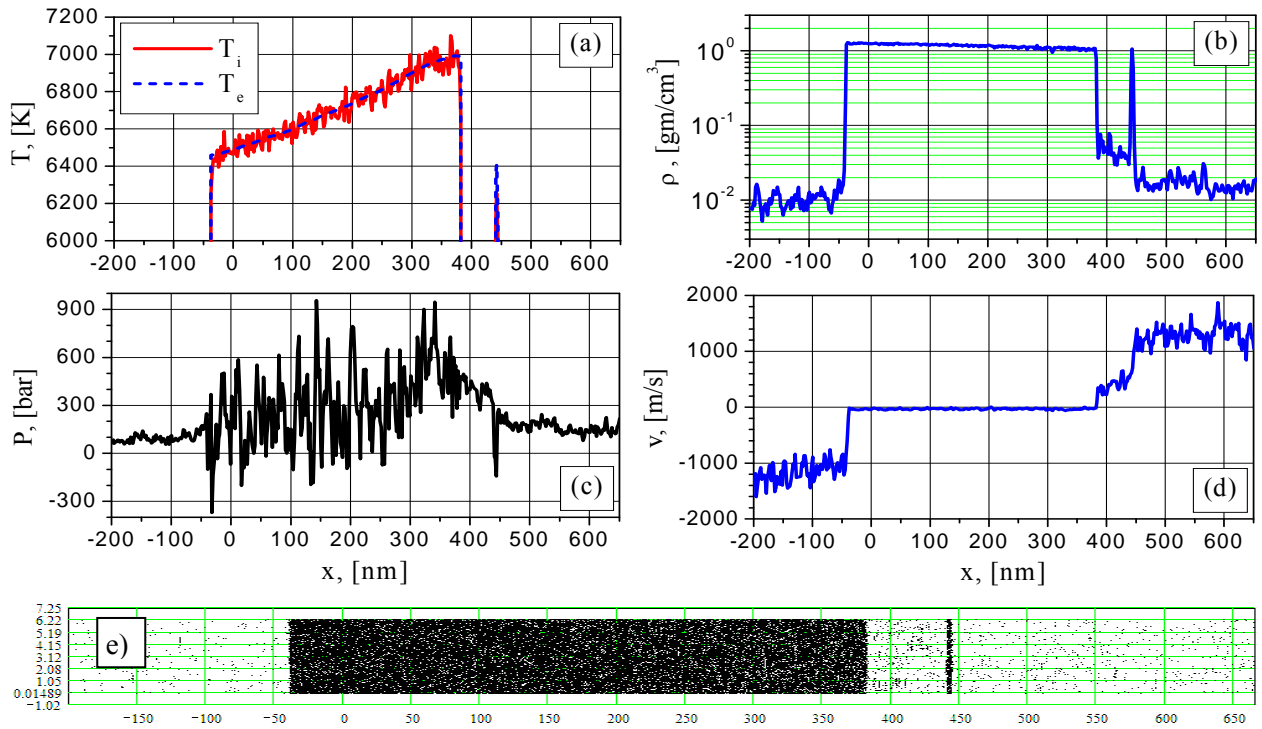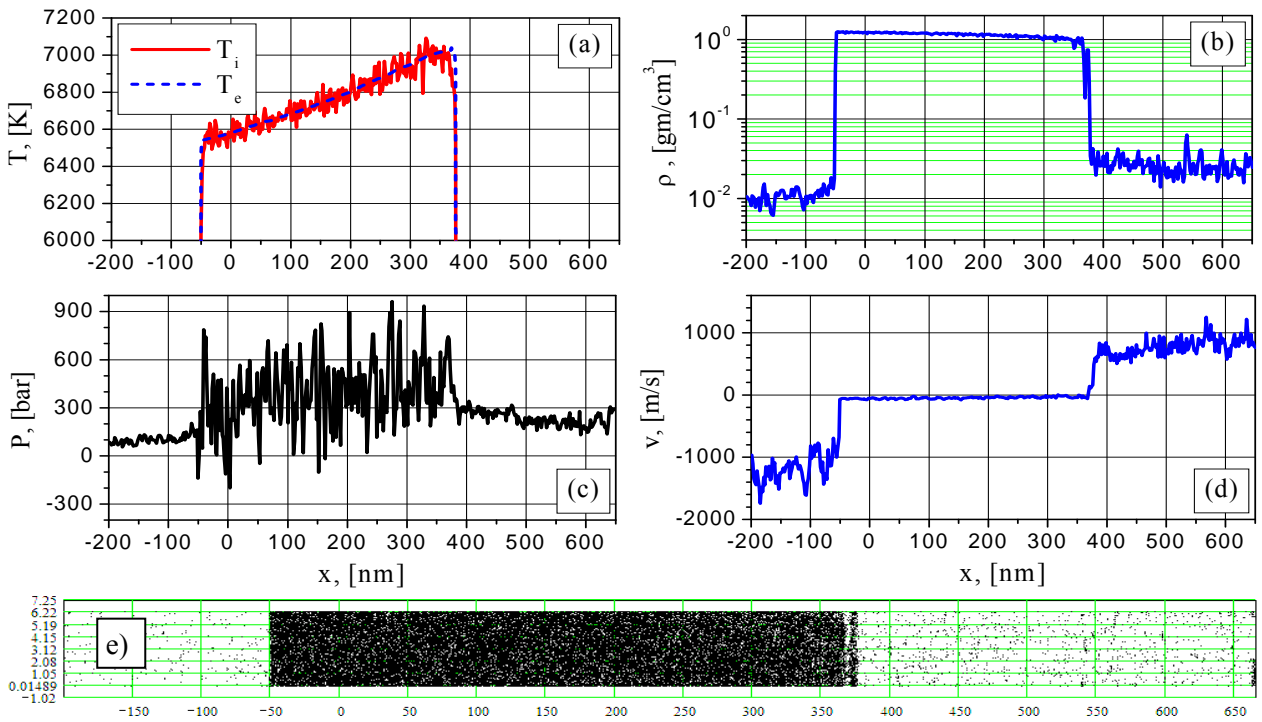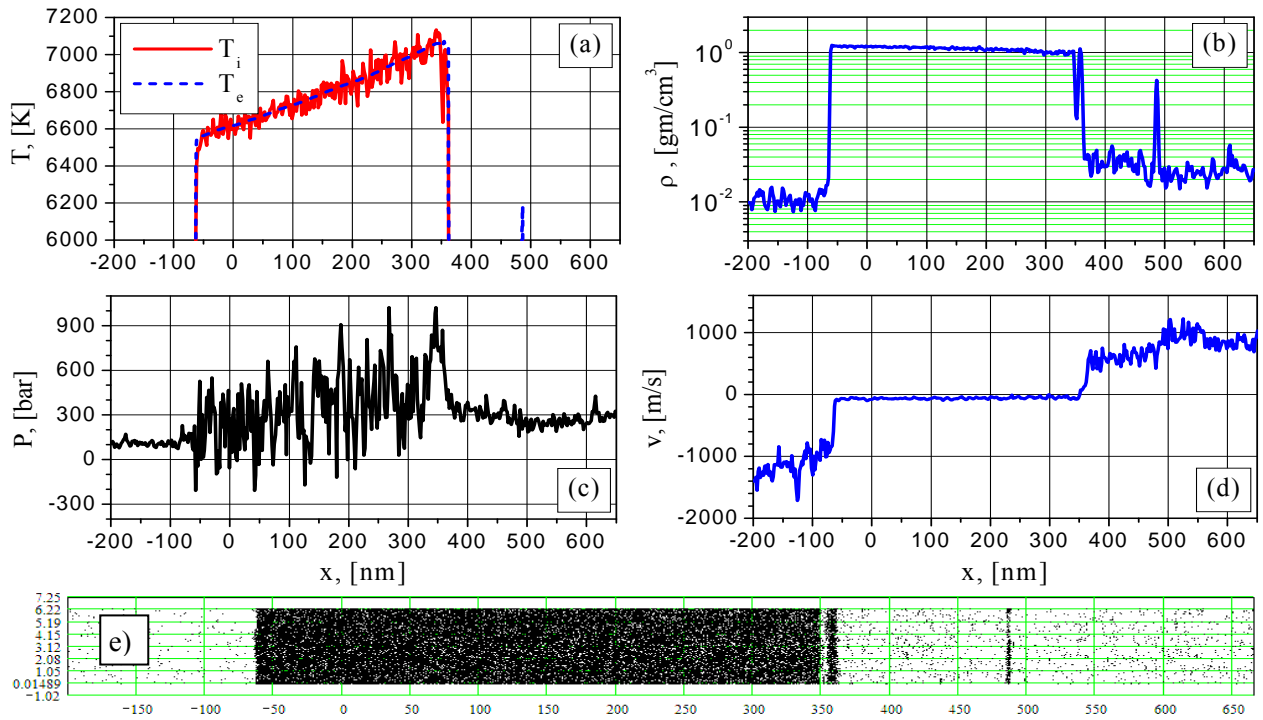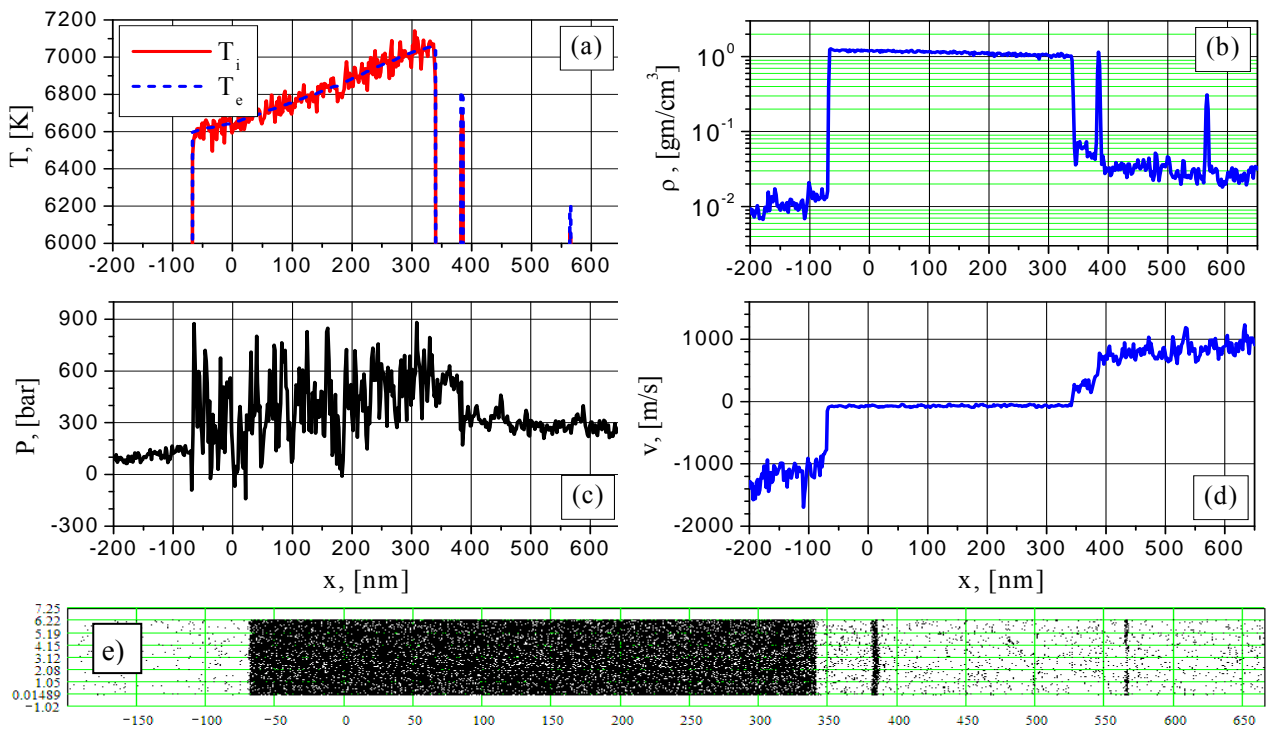Fig.6 Electron and ion temperature (a), density (b), pressure (c), velocity (d) and particle (e) distributions for I =38.5 MW/cm^2 at the time t =1.032 ns: the beginning of explosive boiling.

Fig.7 Electron and ion temperature (a), density (b), pressure (c), velocity (d) and particle (e) distributions for I =38.5 MW/cm^2 at the time t =1.067 ns: separation of the first fragment.
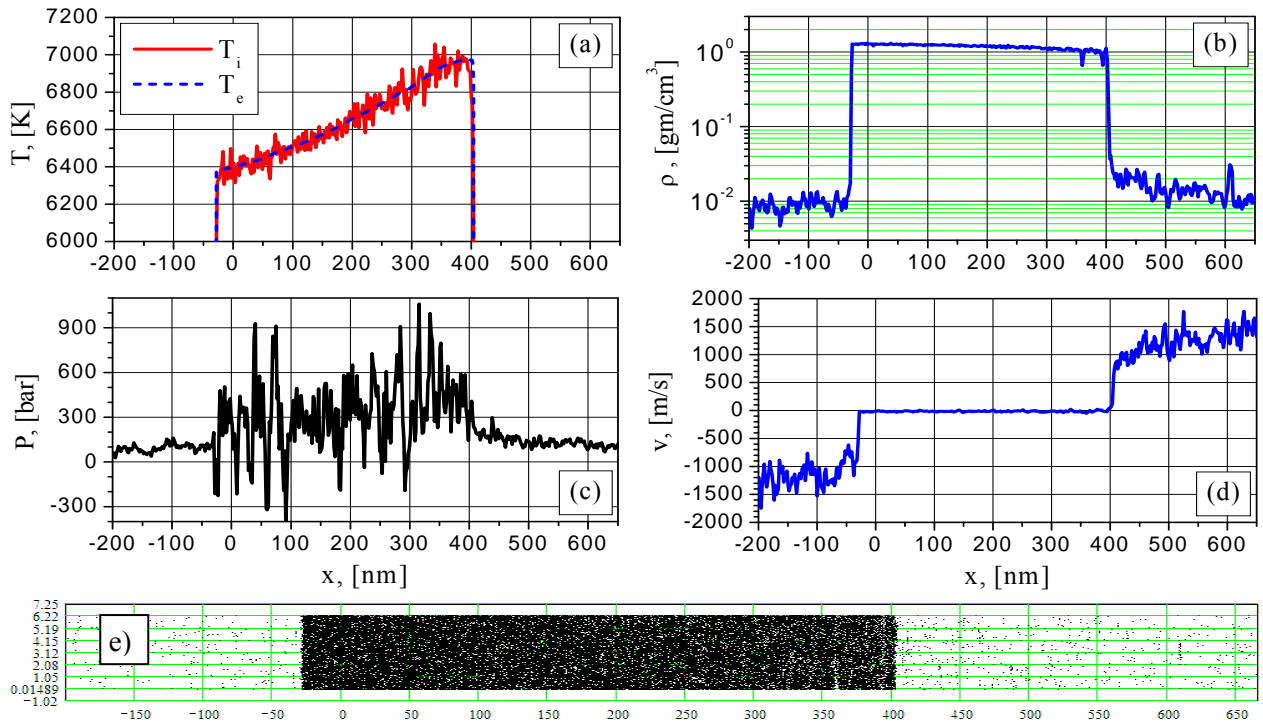
Fig. 8 Electron and ion temperature (a), density (b), pressure (c), velocity (d) and particle (e) distributions for I =38.5 MW/cm^2 at the time t =1.157 ns: velocity and density variations; growth of the fragment density.
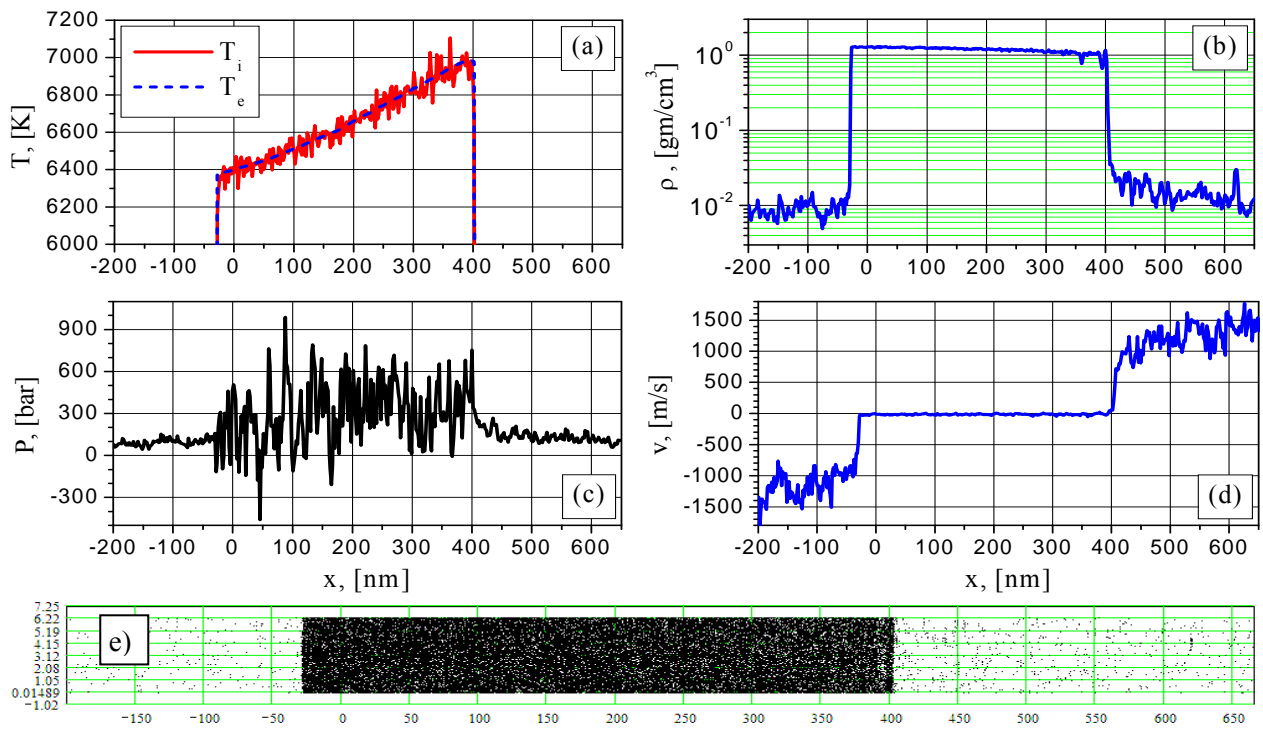
Fig. 9 Electron and ion temperature (a), density (b), pressure (c), velocity (d) and particle (e) distributions for I =38.5 MW/cm^2 at the time t =1.447 ns: second explosive boiling.

Fig. 10 Electron and ion temperature (a), density (b), pressure (c), velocity (d) and particle (e) distributions for I =38.5 MW/cm^2 at the time t =1.657 ns: third explosive boiling.
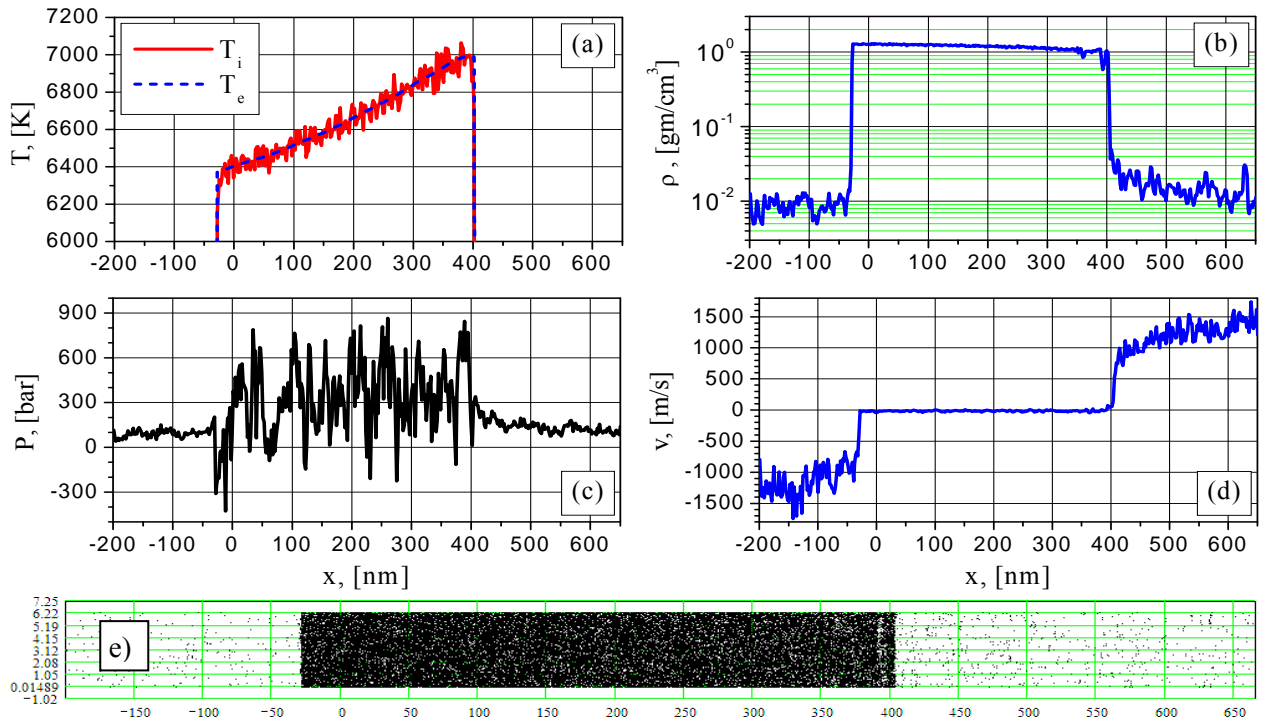

Fig. 11 Electron and ion temperature (a), density (b), pressure (c), velocity (d) and particle (e) distributions for I =38.5 MW/cm^2 at the time t =1.752 ns: velocity and density variations; growth of the fragment density.
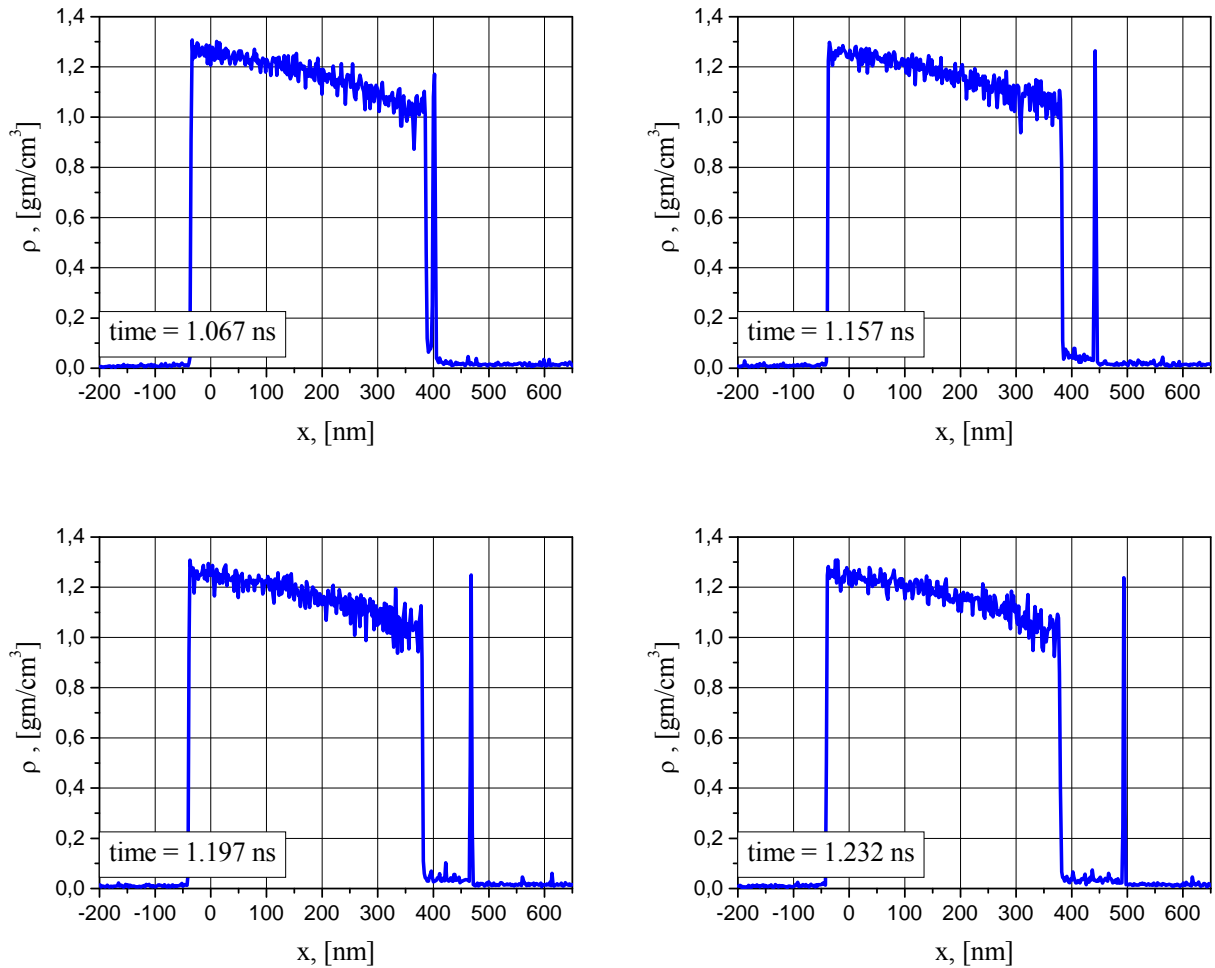
Fig.12 Evolution of the density distribution (linear scale, 1 ps time averaging)) after the first explosion for I =38.5MW/cm^2: growth of the fragment density.
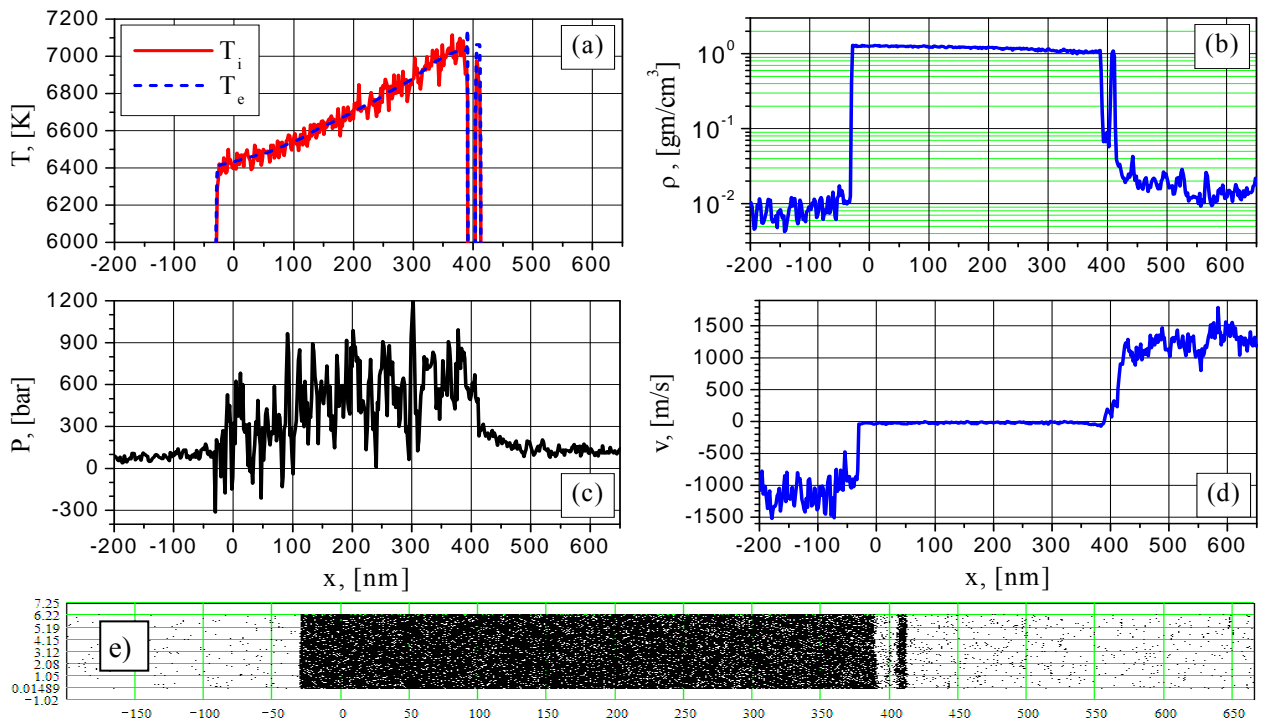
Fig.13 Electron and ion temperature (a), density (b), pressure (c), velocity (d) and particle (e) distributions for I =44MW/cm^2 at the time t = 0.6762 ns: "competition" between the growing fluctuations.

Fig.14 Electron and ion temperature (a), density (b), pressure (c), velocity (d) and particle (e) distributions for I =44MW/cm^2 at the time t =0.6842 ns: "competition" between the growing fluctuations.

Fig.15 Electron and ion temperature (a), density (b), pressure (c), velocity (d) and particle (e) distributions for I =44MW/cm^2 at the time t =0.6942 ns: "competition" between the growing fluctuations.

Fig. 16 Electron and ion temperature (a), density (b), pressure (c), velocity (d) and particle (e) distributions for I =44MW/cm^2 at the time t =0.7622 ns: stabilization of a single fragment.
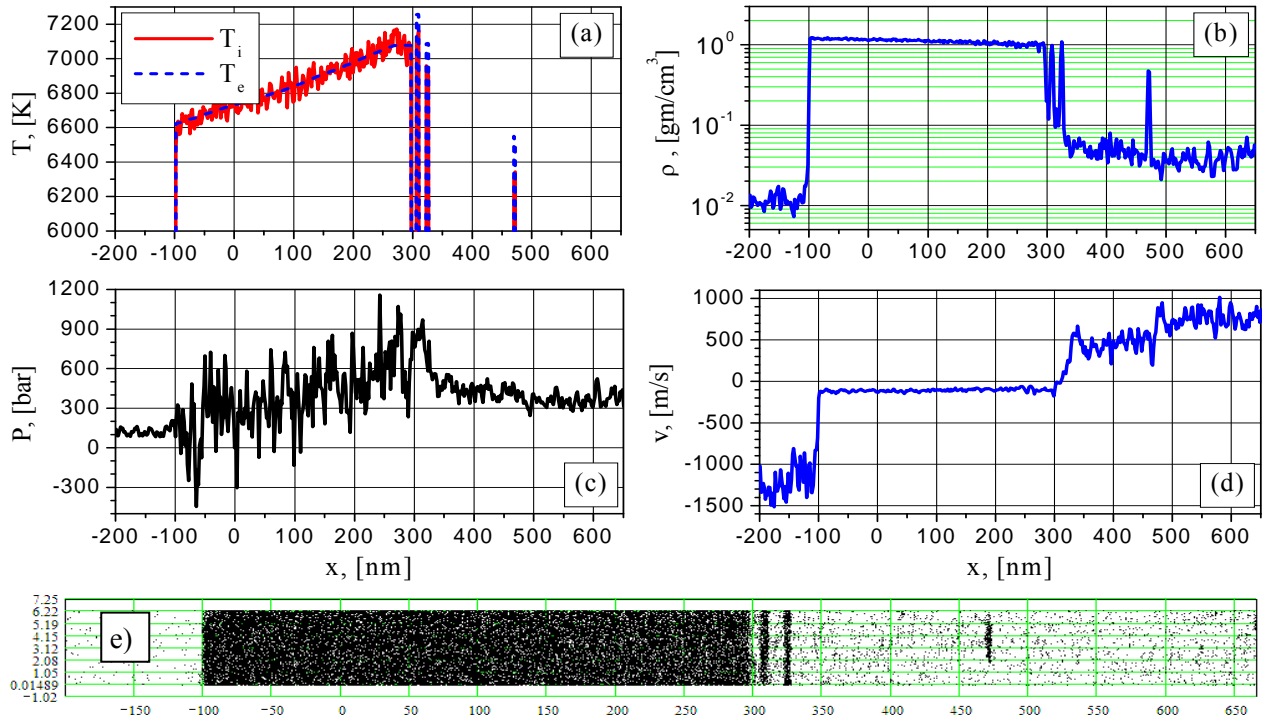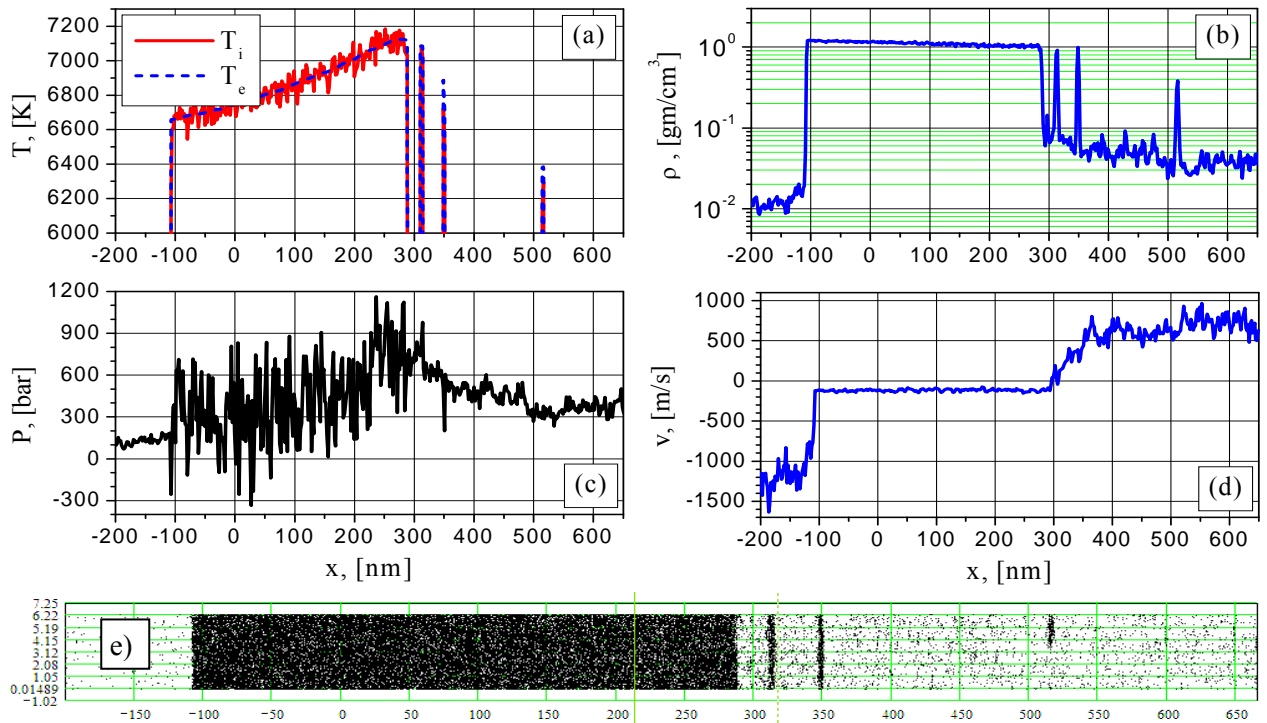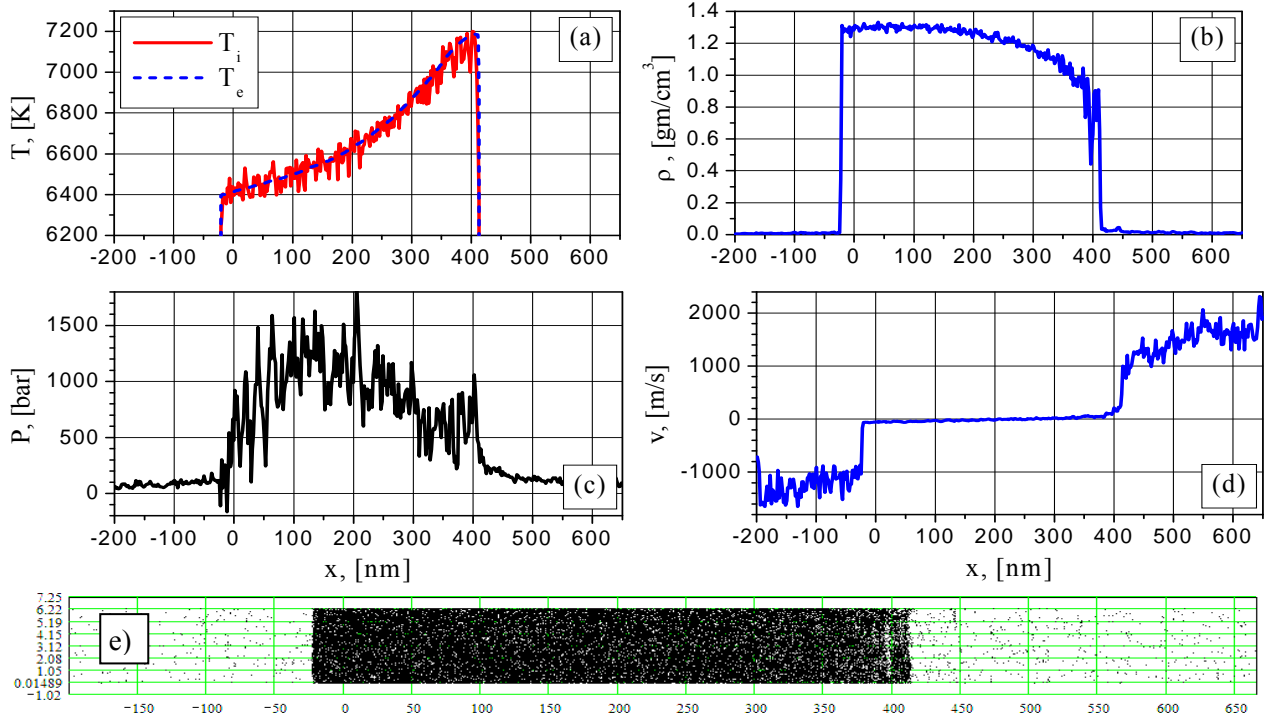
Fig.17 Electron and ion temperature (a), density (b), pressure (c), velocity (d) and particle (e) distributions for I =44MW/cm^2 at the time t = 1.8252 ns: heating continues – several consecutive separated fragments.

Fig.18 Electron and ion temperature (a), density (b), pressure (c), velocity (d) and particle (e) distributions for I =44MW/cm^2 at the time t =1.8982 ns: thinning of the fragments.

Fig.19 Electron and ion temperature (a), density (b), pressure (c), velocity (d) and particle (e) distributions for I =88MW/cm^2 at the time t =0.2252 ns: change from boiling to spinodal decomposition.
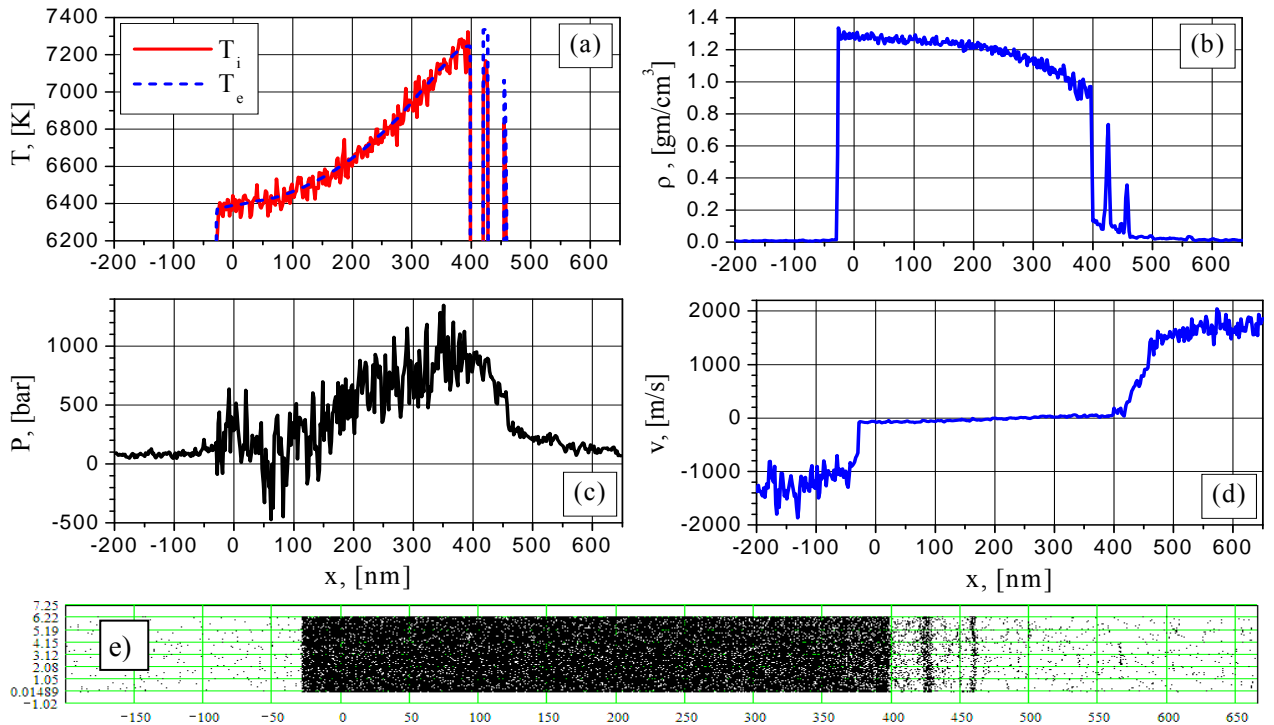

Fig.20 Electron and ion temperature (a), density (b), pressure (c), velocity (d) and particle (e) distributions for I =88MW/cm^2 at the time t = 0.3152 ns: change from boiling to spinodal decomposition.
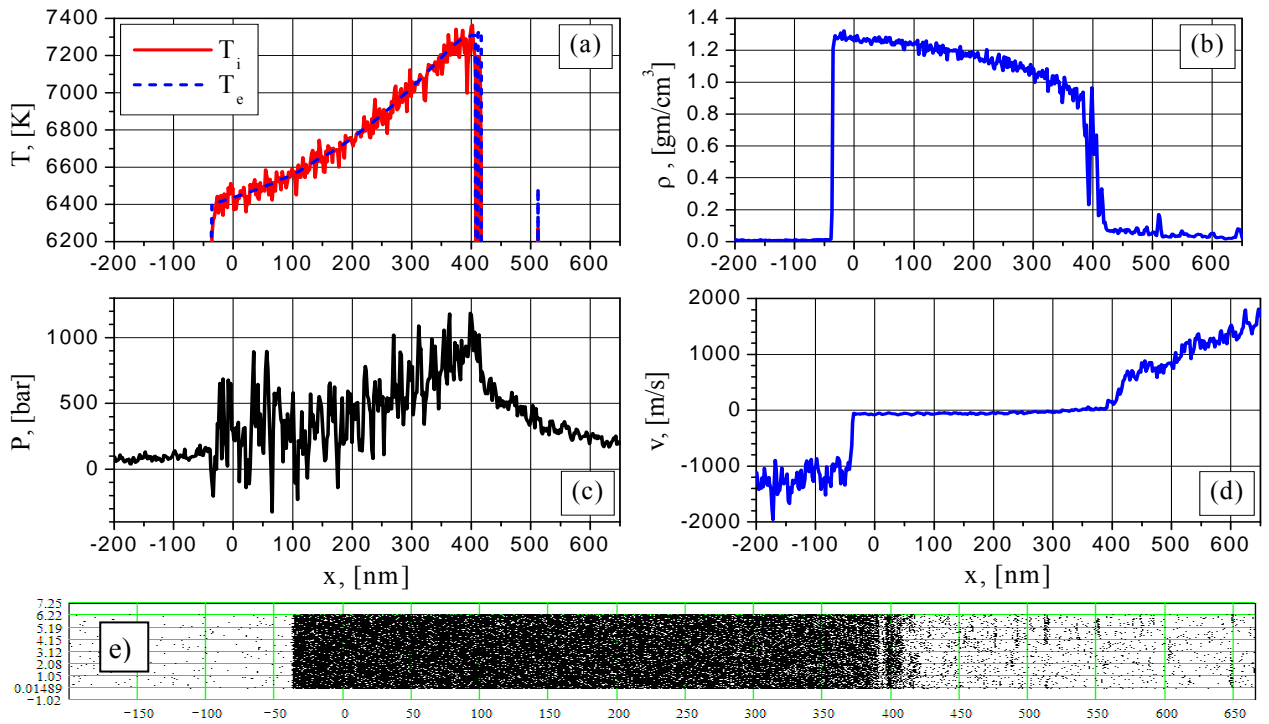
Fig.21 Electron and ion temperature (a), density (b), pressure (c), velocity (d) and particle (e) distributions for I =88MW/cm^2 at the time t =0.4552 ns: change from boiling to spinodal decomposition.
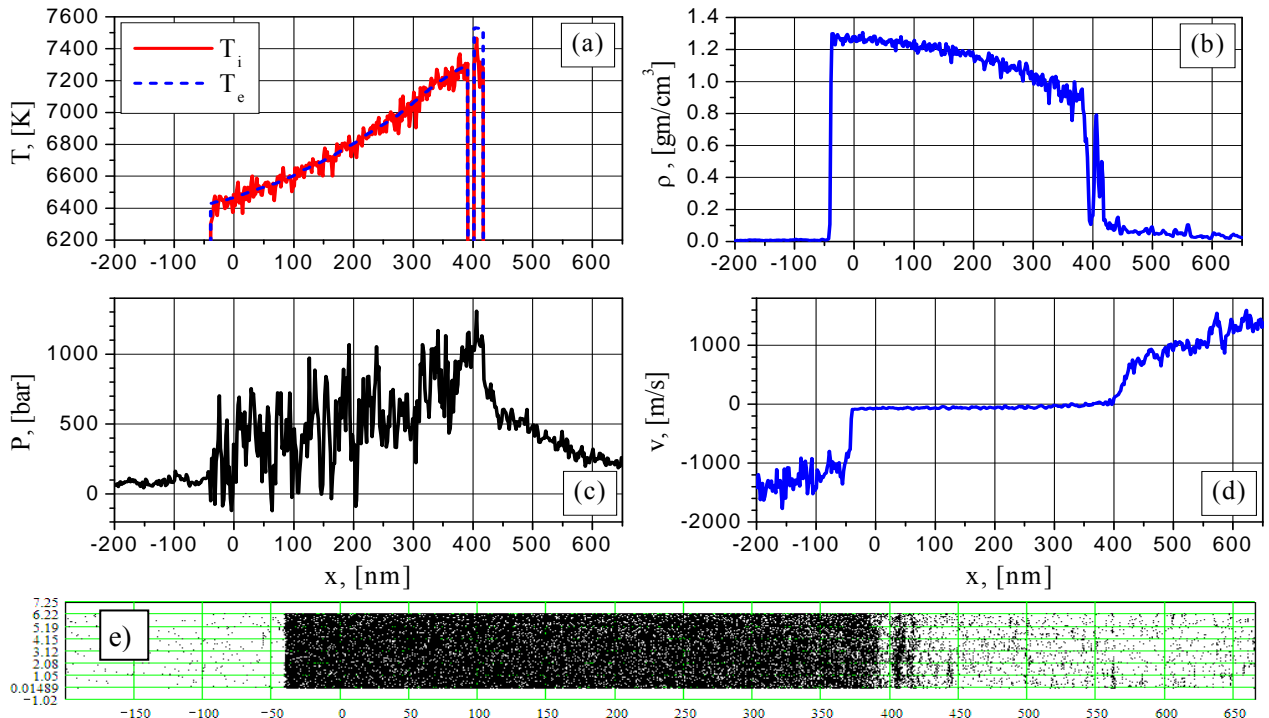

Fig.22 Electron and ion temperature (a), density (b), pressure (c), velocity (d) and particle (e) distributions for I =88MW/cm^2 at the time t =0.5052 ns: change from boiling to spinodal decomposition.

Fig.23 Electron and ion temperature (a), density (b), pressure (c), velocity (d) and particle (e) distributions for I =88MW/cm^2 at the time t =0.7302 ns: spinodal decomposition.
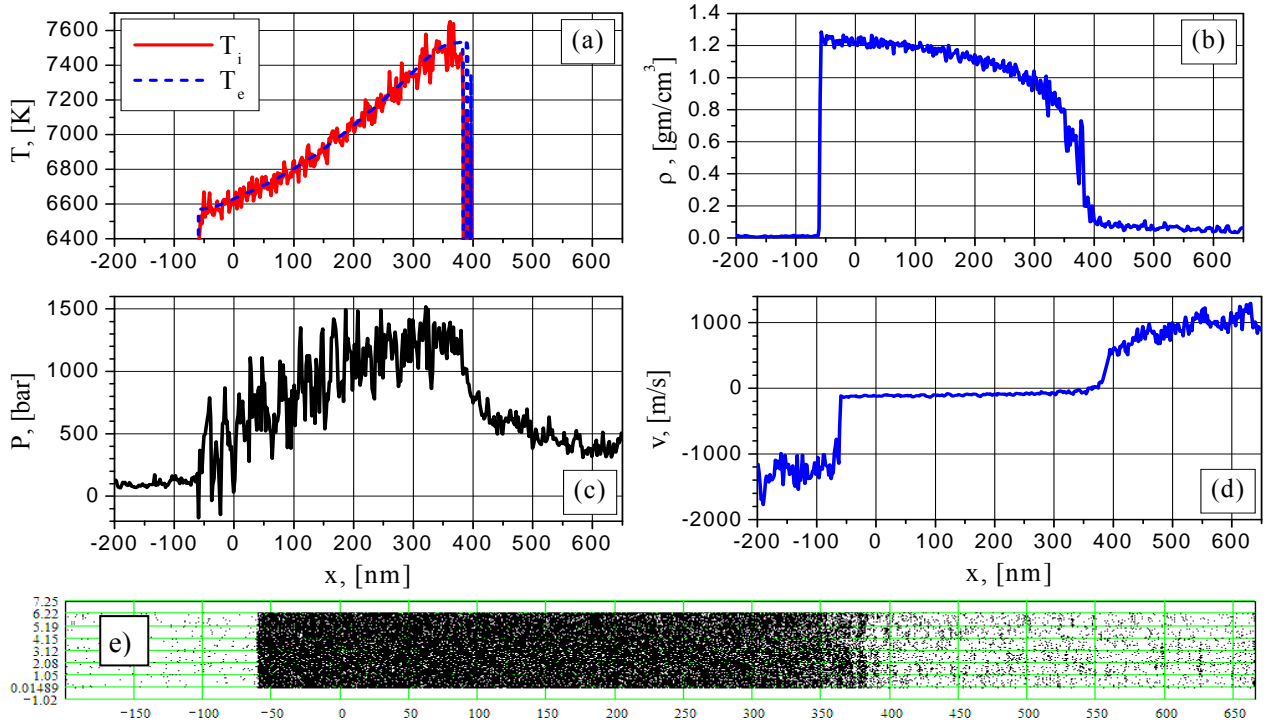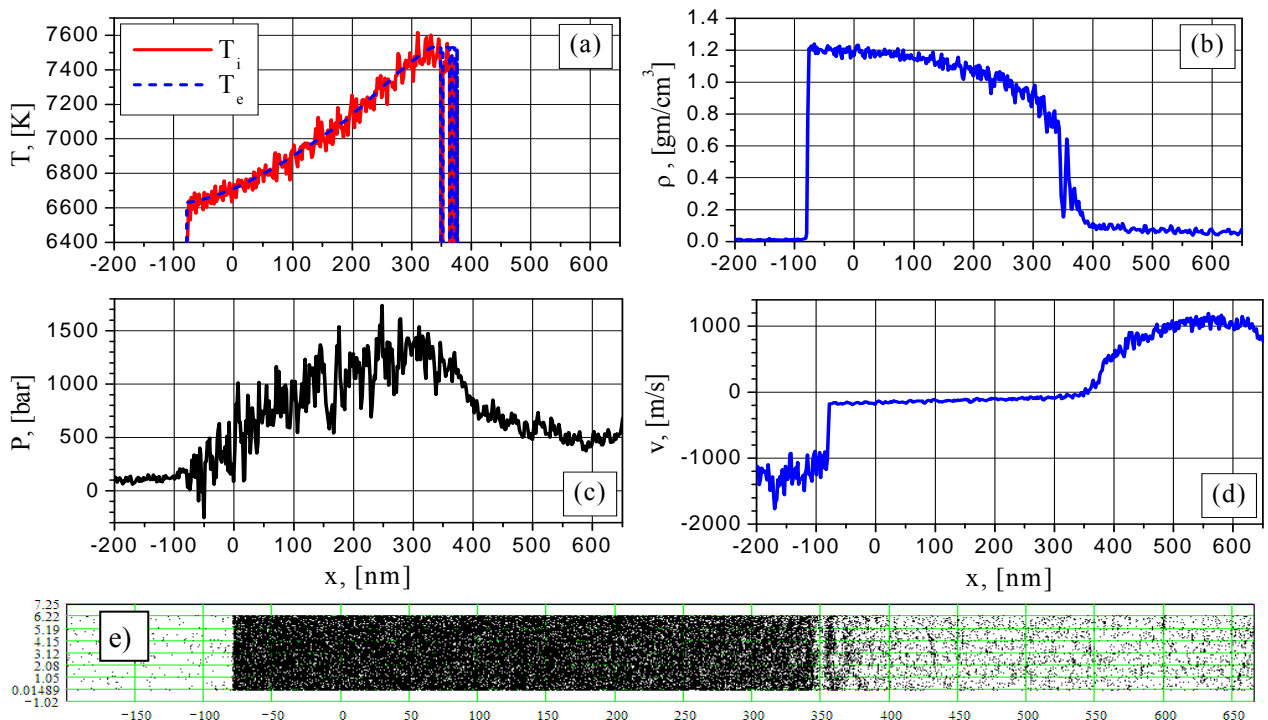

Fig.24 Electron and ion temperature (a), density (b), pressure (c), velocity (d) and particle (e) distributions for I =88MW/cm^2 at the time t =0.8602 ns: spinodal decomposition.

Fig.25 Electron and ion temperature (a), density (b), pressure (c), velocity (d) and particle (e) distributions for I =154 MW/cm^2 at the time t =0.1252 ns: spinodal decomposition without explosive boiling.

Fig.26 Electron and ion temperature (a), density (b), pressure (c), velocity (d) and particle (e) distributions for I =154MW/cm^2 at the time t = 0.1402 ns: spinodal decomposition without explosive boiling.
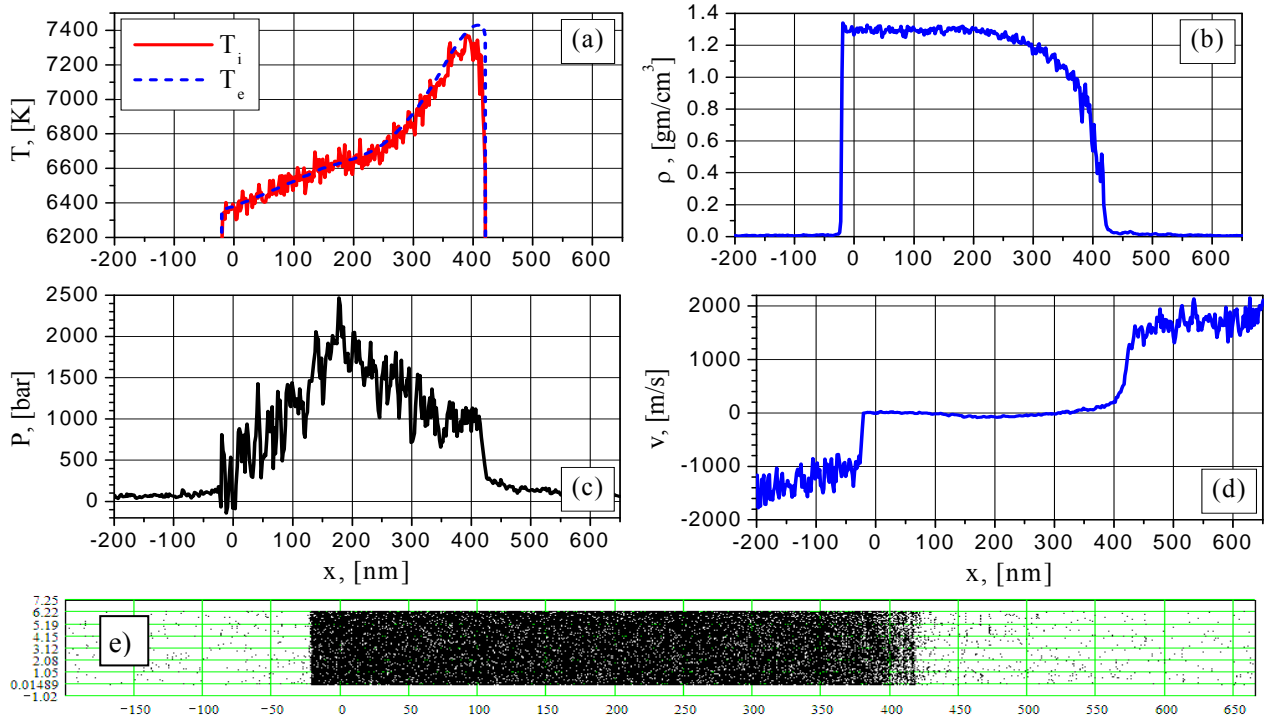
Fig.27 Electron and ion temperature (a), density (b), pressure (c), velocity (d) and particle (e) distributions for I =154MW/cm^2 at the time t = 0.2202 ns: change from spinodal decomposition to supercritical ablation.
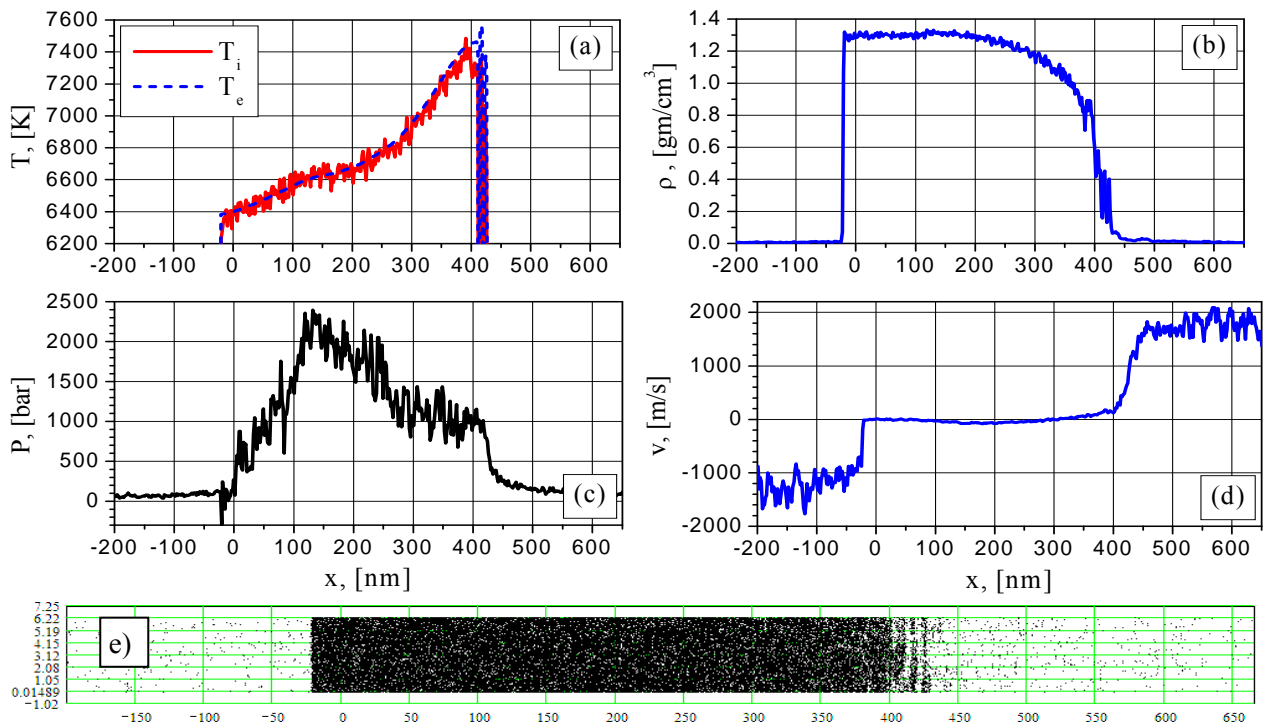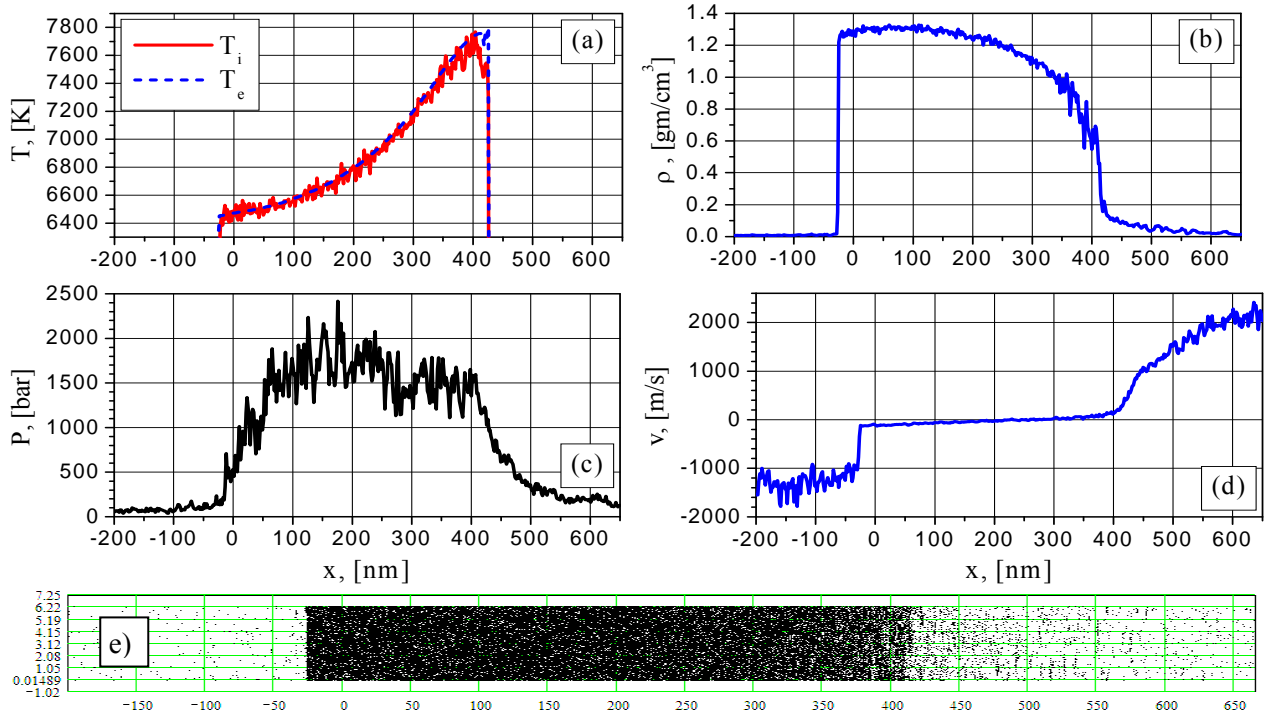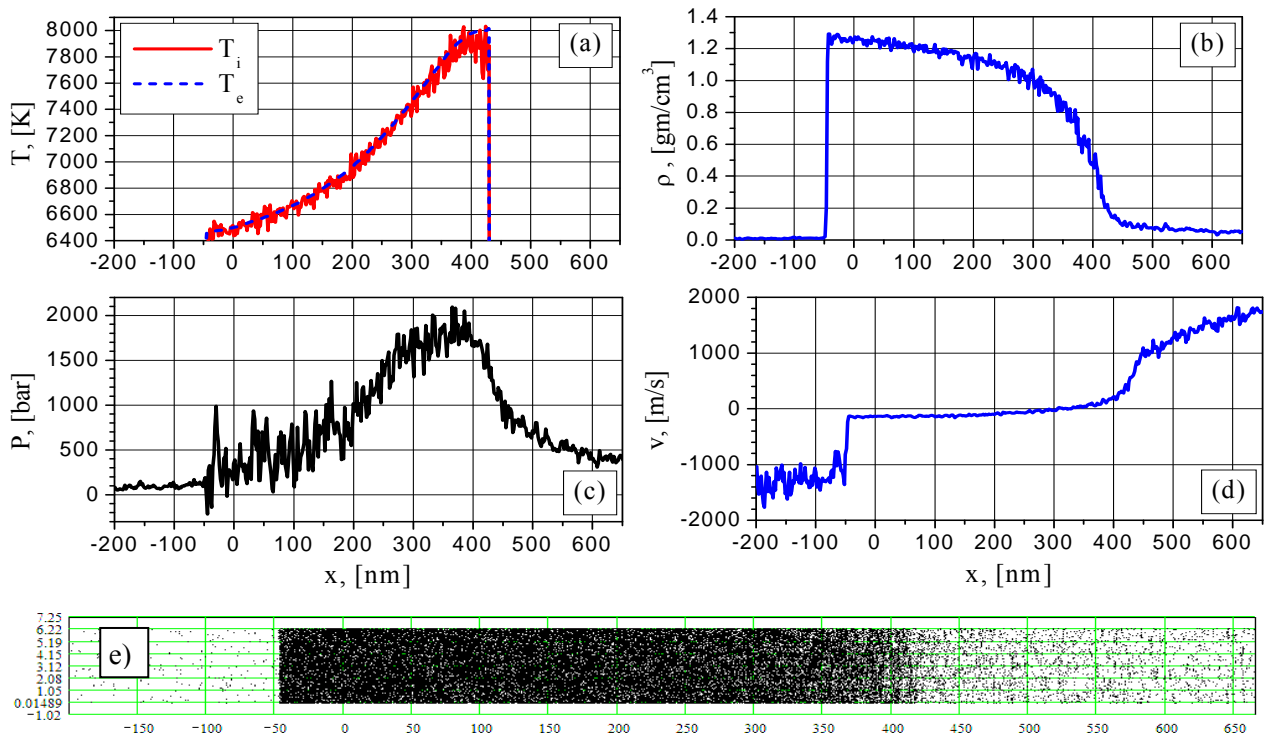

Fig. 28 Electron and ion temperature (a), density (b), pressure (c), velocity (d) and particle (e) distributions for I =154MW/cm^2 at the time t = 0.3752 ns: change from spinodal decomposition to supercritical ablation.

The spinodal decompositiom regime is visible also in Fig. 25-Fig. 26 (154 MW/cm^2), while further heating up to and above the critical point (Fig. 27-Fig. 28) results in the supercritical ablation regime with decreasing density fluctuations on the right film side, which becomes simultaneously more smooth and lengthy in contrast to the subcritical ablation case (Fig. 6-Fig. 26). Because of the fast heating rate no explosive boiling regime is observed at 154 MW/cm^2.

In our calculation, the explosive boiling effect is most pronounced at $I = 38.5$ MW/cm^2. Fig. 29 shows the pressure and temperature behavior during the first explosive boiling in the time interval of $0,8 - 1.3$ ns after the beginning of the laser action. At Fig. 29a, the pressure curve up to $t_1 = 1,04$ ns relates to the vapor phase pressure near the irradiated surface which is smaller than the recoil pressure $P_r \geq 0.5 P_s(T_s)$ where T_s denotes the evaporating surface temperature. $P_s(T_s) = 714$ bar at $T_s = 6830$ K while the calculated pressure value in the sample near its surface (P_r) is about 370 bar. During explosive boiling P_r increases approximately by a maximum of the factor 1.6 (from 370 to 610 bar) remaining somewhat lower than $P_s(T_m) = 802$ bar with $T_m = 6950$ K at the subsurface point x_m where the explosive boiling begins. The temperature jump in Fig. 29b is due to displacement of the observation point from the irradiated surface to the point x_m at t_1 and it corresponds approximately to the temperature difference $(T_m - T_s)$ mentioned above.
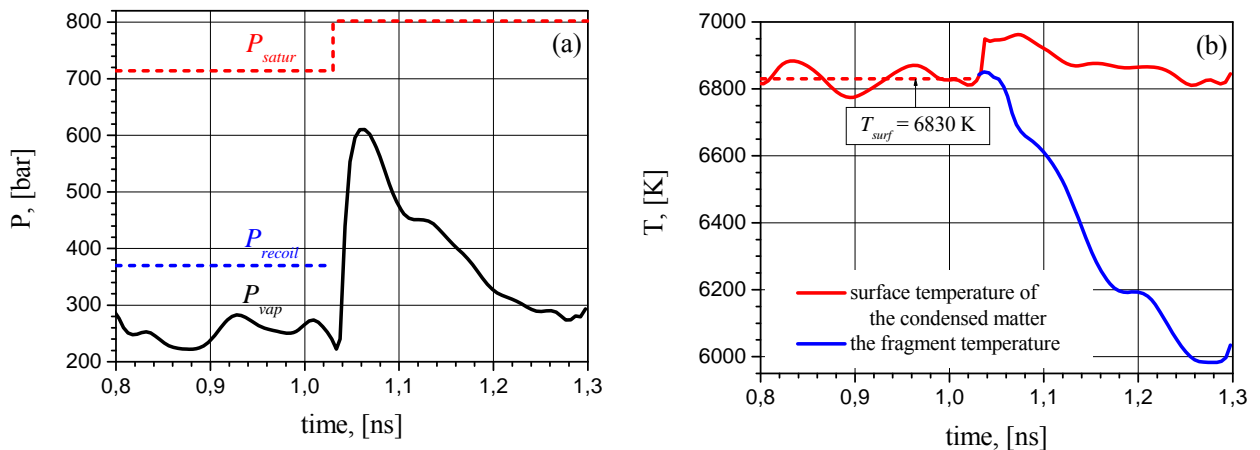
Fig. 29 Pressure (a) and temperature (b) evolution at the surface of the bulk sample (red) and of the fragment (blue) for $I = 38.5$ MW/cm^2

It is interesting to note that in the experiment [15] approximately twofold shock wave pressure rise above the irradiated Al target was detected and interpreted as transition from normal vaporization to phase explosion (explosive boiling). In this case, however, one should also take into account the effects of the plasma formation.

4 CONCLUDING REMARKS

The results of our modeling confirm the possibility to discriminate four different regimes in the nanosecond laser evaporation of metals depending on the laser intensity: quasi-stationary regime with surface evaporation, explosive (volume) boiling, spinodal decomposition and supercritical fluid expansion. The recoil pressure pulsation due to explosive boiling can be used as a marker of the approaching critical parameters values in the irradiated sample while the ablation regime with the critical pressure and temperature values have no such distinctive manifestations. The detailed analysis of the obtained calculation results as well as possible plasma formation effects will be considered elsewhere.

REFERENCES

[1]   V.I. Mazhukin, A.A. Samokhin, A.V. Shapranov, A.Yu. Ivochkin, "Mathematical modeling of non-equilibrium phase transition in rapidly heated thin liquid film", *Mathematica Montisnigri*, **27,** 65 (2013)

[2]   V.I. Mazhukin, A.A. Samokhin, A.V. Shapranov, A.Yu. Ivochkin, Molekuljarno-dinamicheskoe modelirovanie neravnovesnogo fazovogo perehoda zhidkost'-par pri subnanosekundnom odnorodnom nagreve tonkoj plenki, *Applied Physics and Mathematics*, **5**, 3-17 (2013)

[3]   V.I. Mazhukin, A.A. Samokhin, A.V. Shapranov, A.Yu. Ivochkin, "Modelirovanie vzryvnogo vskipanija tonkoy plenki pri odnorodnom subnanosekundnom nagreve." *Matematicheskoe Modelirovanie*, **26,** 125 (2014) (in Russian)

[4]   V.I. Mazhukin, A.A. Samokhin, A.V. Shapranov, A.Yu. Ivochkin, "Modeling of thin film explosive boiling – surface evaporation effect", *12th Int. Conf. On Laser Ablation (Cola 2013) Book of abstracts*, 152 (2013)

[5]   A.A. Samokhin, "Some aspects of the intense evaporation of condensed media by laser radiation", *Sov. J. Quantum Electron.*, **4**, 1144 (1975) Russian version Kvantovaja Elektronika **1**, 2056, (1974).

[6]   V.I. Mazhukin, A.A. Samokhin, A.V. Shapranov, M.M. Demin, "Vzryvnoe vskipanie metallov pod dejstviem nanosekundnogo lazernogo impul'sa", Kvantovaja Elektronika, **44** 283 (2014) (in Russian)

[7]   V.A. Batanov, F.V. Bunkin, A.M. Prokhorov, V.B. Fedorov, "Evaporation of metallic targets caused by intense optical radiation", *Sov. Phys. JETP* **36**, 311 (1973)

[8]   Samokhin A.A "First-order phase transitions induced by laser radiation in absorbing condensed matter", *Proc. Institute of General Physics (USSR: Academy of Sciences)*, **13**, 1 (1990)

[9]   N.M. Bulgakova, A.V. Bulgakov, *Appl. Phys. A*, **73**,199 (2001)

[10] Q. Lu, S. Mao, X. Mao, R. Russo, "Delayed phase explosion during high-power nanosecond laser ablation of silicon", *Appl. Phys. Lett.*, **80**, 3072 (2002)

[11] S.N. Andreev, V.I. Mazhukin, N.M. Nikiforova, A.A. Samokhin, "On possible manifestations of the induced transparency during laser evaporation of metals", *Quantum Electron.*, **33**, 771 (2003)

[12] B.J. Garrison, T.E. Itina, L.V. Zhigilei, "Limit of overheating and the threshold behaviour in laser ablation", *Phys. Rev. B*, **68**, 041501 (2003)

[13] D.S. Ivanov, L.V. Zhigilei, "Combined atomistic-continuum modeling of short-pulse laser melting and disintegration of metal films", *Phys.Rev.B*, **68**, 064114 (2003)

[14] C. Porneala, D.A. Willis, "Effect of the dielectric transition on laser-induced phase explosion in metals", *Int. J. Heat Mass Transfer*, **49**, 1928 (2006)

[15] C. Porneala, D.A. Willis, "Time-resolved dynamics of nanosecond laser-induced phase explosion", *J. Phys. D: Appl. Phys.*, **42**, 155503 (2009)

[16] V.V. Zhakhovskii, N.A. Inogamov, Yu.V. Petrov, S.I. Ashitkov, K. Nishihara, "Two temperature relaxation and melting after absorption of femtosecond laser pulse", *Appl. Surf. Sci.*, **255**, 9592 (2009)

[17] A.A. Ionin, S.I. Kudryashov, L.V. Seleznev, D.V. Sinitsyn, "Nonlinear regime of the excitation of a surface electromagnetic wave on the silicon surface by an intense femtosecond laser pulse", *JETP Lett.* 94, 753 (2011)

[18] A.A. Samokhin, N.N. Il'ichev, S.M. Klimentov, P.A. Pivovarov, "Photoacoustic and laser-induced evaporation effects in liquids", *Appl. Phys. B*, **105**, 551 (2011)

[19] A.A. Ionin, S.I. Kudryashov, L.V. Seleznev, D.V. Sinitsyn, A.F. Bunkin, V.N. Lednev, S.M. Pershin, "Thermal melting and ablation of silicon by femtosecond laser radiation", *JETP*, **116**, 347-362 (2013).

[20] C. Wu, L.V. Zhigilei, "Microscopic mechanisms of laser spallation and ablation of metal targets from large-scale molecular dynamics simulations", *Appl. Phys. A*, **114,** 11-32 (2014)

[21] V.I.Mazhukin. Kinetics and Dynamics of Phase Transformations in Metals Under Action of Ultra-Short High-Power Laser Pulses. Chapter 8, pp.219 -276. In "*Laser Pulses – Theory, Technology, and Applications",* InTech. Ed. by I. Peshko., P 544, (2012).

[22] Ja. I. Frenkel. Kineticheskaja teorija zhidkostejj. L.: Nauka. 592 p. (1975) (in Russian)

[23] V.I. Mazhukin, A.V Mazhukin., O.N. Koroleva. Optical properties of electron Fermi-gas of metals at arbitrary temperature and frequency. *Laser Physics*. **19,** 1179 – 1186 (2009)

[24] W.M. Brown, P. Wang, S.J. Plimpton, A.N. Tharrington, "Implementing molecular dynamics on hybrid high performance computers – short range forces", *Comp. Phys. Commun*., **182**, 898 (2011)